RESEARCH ARTICLE

Check for updates

Hollow Co_3O_4 dodecahedrons with controlled crystal orientation and oxygen vacancies for the high performance oxygen evolution reaction†

Hang Yang,‡ Hui Sun, [ID] ‡ Xiaochen Fan, Xiaozhong Wang,* Qingfeng Yang [ID] and Xiaoyong Lai [ID] *

Rational design and preparation of advanced electrocatalysts for the oxygen evolution reaction (OER) are highly desirable, where various strategies have been applied to enhance the electrocatalytic activities, such as developing nanostructures, facet control, and creating oxygen vacancies. Herein, we have successfully integrated multiple strategies into one catalytic system for further enhancing the OER performance. A series of hollow Co_3O_4 dodecahedrons with controlled crystal orientation and oxygen vacancies were prepared by using ZIF-67 as a precursor and adjusting the atmosphere during calcination. Hollow Co_3O_4 dodecahedrons with both controlled exposure of the (111) facets and high content of oxygen vacancies showed an excellent OER performance with an overpotential of 307 mV at 10 mA cm^{-2} and a Tafel slope as low as 55 mV dec^{-1} and significantly superior to its counterpart with low content of oxygen vacancies or a broken Co_3O_4 dodecahedron being ground and losing the preferred facets of (111). The excellent OER performance should be attributed to the unique hollow structure and the effective control of the (111) facets and oxygen vacancies, which allows for more highly active sites and enhanced conductivity.

1. Introduction

With the continuous excessive consumption of fossil energy, the related energy and environmental issues are increasingly prominent.[1–3] Electrochemical energy storage, such as electrical catalyzed water splitting,[4] nitrogen fixation,[5] and carbon dioxide reduction,[6] are promising strategies to convert redundant electricity into chemical energy.[7–10] The oxygen evolution reaction (OER) is a half reaction of overall water splitting, which plays a critical role in various next-generation energy storage techniques including the use of fuel cells and metal–air batteries.[11–14] The OER is a four electron–proton coupled reaction but far from practical application due to the lack of proper catalysts to promote the sluggish kinetics.[15,16] Iridium and ruthenium oxides are proved to have excellent OER catalytic performance. However, the vulnerable stability and high cost prevent them from wide application in practical production.[17–21]

State Key Laboratory of High-Efficiency Utilization of Coal and Green Chemical Engineering, School of Chemistry and Chemical Engineering, Ningxia University, Yinchuan 750021, People's Republic of China. E-mail: xylai@nxu.edu.cn, xzwang@nxu.edu.cn; Fax: +86-0951-2062323; Tel: +86-0951-2061456

† Electronic supplementary information (ESI) available: XRD patterns, nitrogen adsorption–desorption isotherms, EDS spectra, XPS spectra and electrochemical measurement results. See DOI: 10.1039/d0qm00671h

‡ These authors contributed equally to this work.

Cobalt-based compounds, such as oxides and hydroxides, are regarded as active non-precious metal-based OER catalysts with relatively low cost and easy availability.[22–26] Among them, Co_3O_4 has been frequently investigated due to its considerable OER activity and corrosion resistance in alkaline solution,[27–30] although its bulk material is less active for the OER because of the limited surface area and conductivity. Therefore, various strategies have been applied to enhance the OER activity of Co_3O_4, such as developing nanostructured materials for increasing surface area, facet control for generating more highly active sites,[31–33] creating oxygen vacancies for regulating electronic states and improving conductivity.[30] For instance, Gupta *et al.*[25] reported a flower-shaped Co_3O_4 nanostructure showing a low overpotential of 356 mV at 10 mA cm^{-2} with a Tafel slope of 68 mV dec^{-1}. Liu *et al.*[34] synthesized four types of Co_3O_4 nanocrystals by predominantly exposing (111), (112), (110) and (001) facets, respectively, and illustrated the highest OER activity of the Co_3O_4 nanocrystals with exposed (111) facets due to the highest surface energy, largest dangling bond density and smallest free energy. Xu *et al.*[35] presented a plasma-engraving strategy to create more oxygen vacancies on Co_3O_4 nanosheets and thus resulted in a higher atomic ratio of Co^{2+}/Co^{3+} (1.2) than that (1.0) of those without plasma-engraving, which substantially improves the electronic conductivity and generates more active defects for the OER. Nevertheless, these strategies are still expected to be combined into one catalytic

system for further enhancing the OER performance, which remains a great challenge.

Hollow nanostructures possess some unique advantages for practical application in wide fields,[28,36–50] such as high specific surface area, abundant active sites, and multiple mass-transferring channels. Among all the methods for fabricating hollow structured materials, the self-templating methods based on metal–organic frameworks (MOFs) are receiving more and more attention.[51–57] For example, Yao and coworkers[58] prepared a hollow Co_3O_4/C OER electrocatalyst through a simple two-step thermal cracking process by using the cobalt ion enriched MOF as a precursor, which exhibited a low over-potential of 349 mV at 10 mA cm^{-2} and a low Tafel slope of 60 mV dec^{-1}, showing a better performance of hollow structures compared to its solid counterpart. Recently, Wang and coworkers[59] first reported a hollow multi-shelled Co_3O_4 dodecahedron templated from zeolitic imidazolate framework-67 (ZIF-67), which showed a dominant exposure of (111) facets and 3 times higher photocatalytic activity toward the reduction of CO_2 than that of its counterpart without facet control. Additionally, our previous work showed that such a hollow Co_3O_4 dodecahedron with dominant exposure of (111) facets could be also used as a promising electrocatalyst for glucose oxidation.[28] However, its direct use for the OER is rarely reported, which should deserve more attention.

Herein, we have prepared a series of hollow Co_3O_4 dodeca-hedrons with controlled crystal orientation and oxygen vacancies using ZIF-67 as a precursor and attempted to combine multiple strategies into one catalytic system for further enhancing the OER performance, as shown in Scheme 1. By finely adjusting the atmosphere (the volume ratio of argon to oxygen, V_{Argon}/V_{Oxygen}) during calcination, hollow Co_3O_4 dodecahedrons with controlled exposure of the (111) facets and high content of oxygen vacancies could be obtained, which substantively

resulted in both an increased electrochemical active surface area (ECSA) and enhanced conductivity. As a result, a better OER performance with an overpotential of 307 mV at 10 mA cm^{-2} and a Tafel slope as low as 55 mV dec^{-1} were realized by using hollow Co_3O_4 dodecahedrons obtained at a relatively low oxygen partial pressure ($V_{Argon}/V_{Oxygen} = 9:1$), which is signifi-cantly superior to those for its counterpart with low content of oxygen vacancies obtained at a relatively high oxygen partial pressure ($V_{Argon}/V_{Oxygen} = 7:2$) or broken Co_3O_4 dodecahedrons being ground and losing the preferred facets of (111).

2. Experimental section

2.1. Materials

Cobalt(II) nitrate hexahydrate ($Co(NO_3)_2 \cdot 6H_2O$, >99.0%) and 2-dimethyl imidazole and potassium hydroxide (KOH, AR) were purchased from Aladdin Reagent. Methanol, anhydrous ethanol and other solvents were obtained from Sinopharm chemical reagent Co., Ltd (Shanghai, China). All reagents were used without further purification. High purity argon and oxy-gen were purchased from Yinchuan Jinfeng Ningfeng Oxygen Co., Ltd (Yinchuan, China). Ultrapure water with a resistivity of 18 MΩ was used in all experiments.

2.2. Synthesis of ZIF-67

In a typical procedure, 22.5 mmol of $Co(NO_3)_2 \cdot 6H_2O$ and 96.9 mmol of 2-dimethyl imidazole were dissolved in a mixture of 60 mL of methanol and 60 mL of ethanol, respectively. Then the solution of 2-dimethyl imidazole was poured into the solution of $Co(NO_3)_2$, and the mixed solution was aged for 24 hours at 40 °C. After centrifugation, the purple precipitate was obtained and dried under vacuum for 24 hours.

2.3. Synthesis of hollow Co_3O_4 dodecahedrons

The hollow Co_3O_4 dodecahedrons were obtained by the calcina-tion of ZIF-67 in a tube furnace under different atmospheres. In a typical method, the tube furnace was purged by mixed gases (the V_{Argon}/V_{Oxygen} values were 7:2, 4:1 and 9:1, respectively) for 30 min before calcination. Then the temperature was raised to 425 °C with a heating rate of 0.5 °C and annealed for 1 hour.

2.4. Characterizations

The surface morphology of ZIF-67 was observed using a ZEISS EVO 18 scanning electron microscope (SEM) with an accelera-tion voltage of 15 kV. Transmission electron microscopy (TEM) images of hollow Co_3O_4 dodecahedrons were obtained using a Hitachi HT-7700 electron microscope with an operating voltage of 120 kV. High-resolution TEM images, selected area electron diffraction (SAED), high-angle annular dark field scanning TEM (HAADF-STEM) images and elemental mappings were recorded by an FEI Talos 200S electron microscope operated at 200 kV. The powder X-ray diffraction (XRD) patterns were recorded on an AXS D8 ADVANCE A25 diffractometer with an operating voltage of 40 kV and a scanning speed of 5° min^{-1}. The nitrogen adsorption–desorption isotherms under liquid
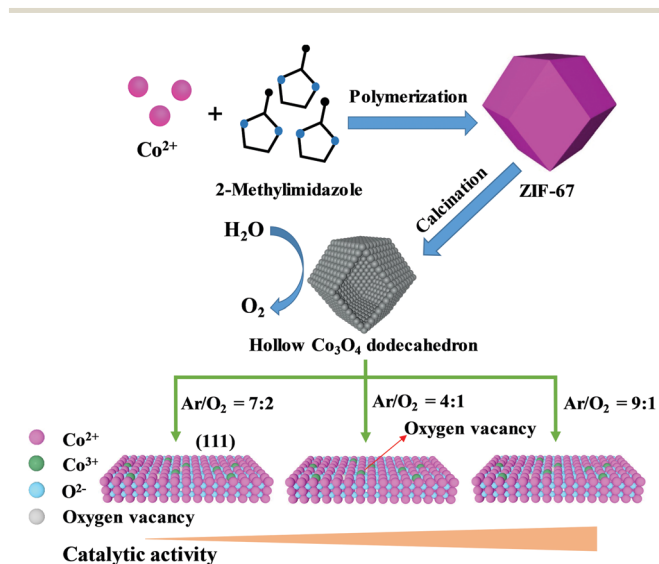
Scheme 1 Schematic of the preparation of hollow Co_3O_4 dodecahe-drons and oxygen content controlled dominant exposure of the (111) facet and oxygen vacancies for the high performance OER.

260 | *Mater. Chem. Front.*, 2021, **5**, 259–267

This journal is © The Royal Society of Chemistry and the Chinese Chemical Society 2021

nitrogen (−196 °C) were measured on the Autosorb iQ adsorption analyzer. Thermo Scientific ESCALAB 250Xi X-ray photoelectron spectroscopy (XPS) was used to observe the chemical environment of the samples.

2.5. Electrochemical measurements

The electrochemical properties of the samples were determined by a PINE electrochemical workstation (Pine Research Instrumentation, USA) using a conventional three-electrode system. The rotation speed of the rotating-disk electrode (RDE) was set at 1600 rpm, and the disk electrode (RDE 5 mm) deposited with the samples was used as the working electrode, the Ag/AgCl electrode as the reference electrode and the Pt wire electrode as the counter electrode. Before testing, the disk electrode was polished by Al_2O_3 particles with different meshes, and the electrolyte (1 M KOH aqueous solution) was purged by argon for 30 min. The samples (3 mg) were dispersed in 1 mL of anhydrous ethanol under ultrasound treatment for 30 min. Then, 5 μL of the dispersions were dropped on the surface of the disk electrode and dried under ambient temperature conditions. This process was repeated 5 times, so 25 μL of the dispersions were deposited on the surface of the working electrode. Finally, 5 μL of 5 wt% Nafion solution was dropped as a binder on the surface of the electrodes.

The turnover frequency (TOF) calculation:[29] the values of TOF were calculated by using the following equation: TOF = $(j \times S)/(4 \times F \times n)$, where j (mA cm^{-2}) is the measured current density at an overpotential of 300 mV, S is the working surface area of the glassy carbon electrode, the number 4 means a four-electron OER, F is Faraday's constant (96485.3 C mol^{-1}), and n is the moles of the coated Co atom on the electrode calculated from the loading weight and the molecular weight of the coated catalysts (Co_3O_4).

3. Results and discussion

Hollow Co_3O_4 dodecahedrons were synthesized using ZIF-67 as a precursor, which was prepared using a typical procedure.[59] As shown in Fig. 1a, the SEM image indicates the dodecahedron morphology of ZIF-67 with a uniform size of 2.5 μm. The XRD pattern in Fig. S1 (ESI†) further confirms the crystal structure of ZIF-67. After calcination in a mixture of argon and oxygen, the dodecahedron morphology of ZIF-67 was well-preserved to give samples of Co_3O_4-7:2, Co_3O_4-4:1 and Co_3O_4-9:1 based on the value of V_{Argon}/V_{Oxygen}. The TEM images in Fig. 1b–d demonstrate the hollow structure of Co_3O_4-7:2, Co_3O_4-4:1 and Co_3O_4-9:1 with a similar size of about 1.2 μm. Instead of the smooth surface of ZIF-67, the shell of the Co_3O_4 dodecahedrons was composed of small Co_3O_4 nanoparticles, resulting in a rough surface and high specific areas of about 36 m^2 g^{-1}, as illustrated in Fig. S2, (ESI†).

In order to investigate the detailed microstructure of the synthesized Co_3O_4 dodecahedrons, HR-TEM was performed to observe the crystal structure and chemical composition of Co_3O_4-9:1. As illustrated in Fig. 2a, the shell of the Co_3O_4-9:1
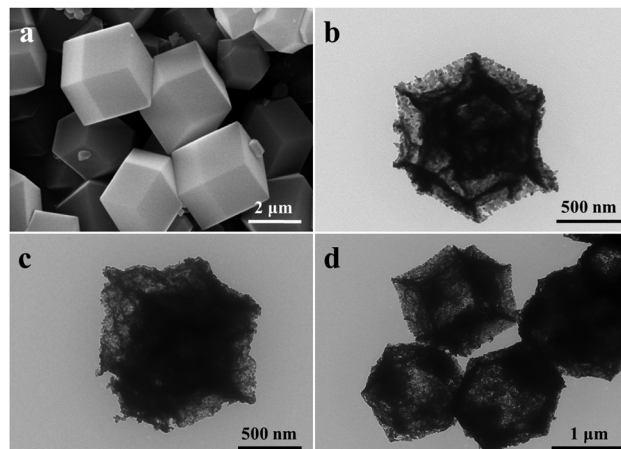

Fig. 1 (a) SEM image of ZIF-67 and (b–d) TEM images of Co_3O_4-7:2, Co_3O_4-4:1 and Co_3O_4-9:1, respectively.

dodecahedron was formed of small Co_3O_4 nanoparticles with various morphologies. The average diameter of the Co_3O_4 nanoparticles is measured to be 22.3 ± 5.4 nm. The crystal facet of the spinel Co_3O_4 was determined by calculating the crystal plane spacing based on the HR-TEM image in Fig. 2b. The d-spacings of 0.462, 0.246 and 0.285 nm are ascribed to the (111), (311) and (220) planes, respectively. Besides, the SAED pattern in Fig. 2c also indicates the polycrystalline structure of the Co_3O_4 nanoparticles. The content of all elements of Co_3O_4-9:1 can be determined by EDS (Fig. S3, ESI†), and the atomic fraction of Co and O is 38.4% and 55.0%, in accordance with the stoichiometric ratio of Co_3O_4. Moreover, there is also residual carbon with an atomic fraction of 4.7%, which might increase the conductivity of the samples. The HAADF-STEM image and elemental mappings in Fig. 2d–f reveal the homogeneous distribution of Co and O elements.

It has been reported that the (111) plane dominant Co_3O_4 hollow multi-shell structures could be obtained by the calcination of ZIF-67 due to the topological arrangement of metal atoms in ZIF-67, which exhibited significantly enhanced catalytic activity
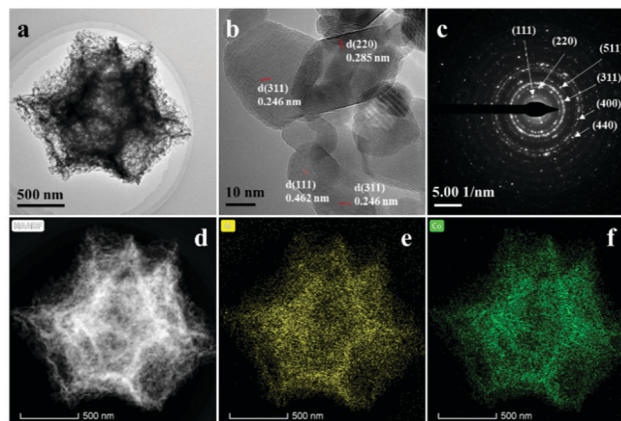

Fig. 2 (a) TEM, (b) HR-TEM image and (c) SAED of Co_3O_4-9:1; (d) HAADF-STEM image and (e and f) elemental mappings of Co_3O_4-9:1.
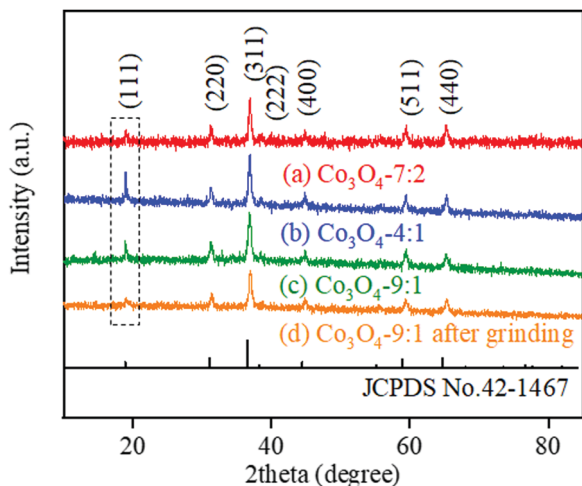
This journal is © The Royal Society of Chemistry and the Chinese Chemical Society 2021

Mater. Chem. Front., 2021, **5**, 259–267 | **261**

Fig. 3 XRD patterns of (a) Co_3O_4-7:2, (b) Co_3O_4-4:1, (c) Co_3O_4-9:1 and (d) Co_3O_4-9:1 after grinding.

for CO_2 photoreduction.[59] Besides, the (111) plane also showed excellent catalytic performance toward the OER.[34,60] Therefore, we changed the calcination conditions to control the exposure of the (111) plane by changing the oxygen partial pressure during calcination. As shown in Fig. 3, XRD analysis was carried out to probe into the crystal structure of the Co_3O_4-7:2, Co_3O_4-4:1 and Co_3O_4-9:1. The main diffraction peaks of (111), (220), (311), (222), (400), (511) and (440) planes are observed, which is in good accordance with the standard card and previous report.[61] However, the intensity of the (111) plane of Co_3O_4-4:1 and Co_3O_4-9:1 is abnormally strong ($I_{(111)}/I_{(311)}$ = 0.61, 0.42, respectively) compared to that of the (311) plane (curve (b) and c) in Fig. 3). When the oxygen partial pressure increased to 7:2,

the selective exposure of the (111) facet disappeared, as shown in Fig. 3a. Besides, the orientation of the (111) facet also disappeared after grinding (Fig. 3d), demonstrating the importance of the hollow dodecahedron structure to maintain the selective exposure of the (111) facet. A previous study has also demonstrated that the dominant exposure of the (111) facet of hollow Co_3O_4 dodecahedrons was the result of the orientated growth and alignment of Co_3O_4 nanocrystals during the shell formation induced by the precursor ZIF-67.[59] The calcination atmosphere might influence the oriented growth and arrangement of the Co_3O_4 nanocrystals.

To evaluate the difference of the surface components and the chemical environment of the elements of hollow Co_3O_4 dodecahedrons with different dominant exposure of the (111) plane, XPS was carried out. The survey XPS spectra in Fig. S4 (ESI†) confirmed the existence of Co, O and C in the samples, while the similar C 1s high resolution XPS spectra of Co_3O_4-7:2, Co_3O_4-4:1 and Co_3O_4-9:1 could be divided into three peaks, belonging to C=C/C–C (284.8 eV), C–O (286.3 eV) and C=O (288.8 eV), as shown in Fig. S5 (ESI†). Fig. 4a–c show the high resolution XPS spectra of Co 2p of Co_3O_4-7:2, Co_3O_4-4:1 and Co_3O_4-9:1, respectively, which present two prominent peaks at 780.2 and 795.1 eV, assigned to the Co $2p_{3/2}$ and Co $2p_{1/2}$ peaks, respectively. The Co $2p_{3/2}$ peak could be subdivided into two peaks centred at 779.6 and 780.4 eV, which were the characteristic peaks of Co^{3+} $2p_{3/2}$ and Co^{2+} $2p_{3/2}$, respectively. Similarly, the Co $2p_{1/2}$ peak could also be subdivided into two peaks that belonged to Co^{3+} $2p_{1/2}$ (794.7 eV) and Co^{2+} $2p_{1/2}$ (796.1 eV), respectively.[62–64] Calculating from the peak area of Co^{3+} and Co^{2+}, the relative content of Co^{2+} of Co_3O_4-9:1 was as high as 75.9%, while the content of Co^{2+} of Co_3O_4-4:1 and Co_3O_4-7:2 was slightly reduced to 72.1% and 71.9%,
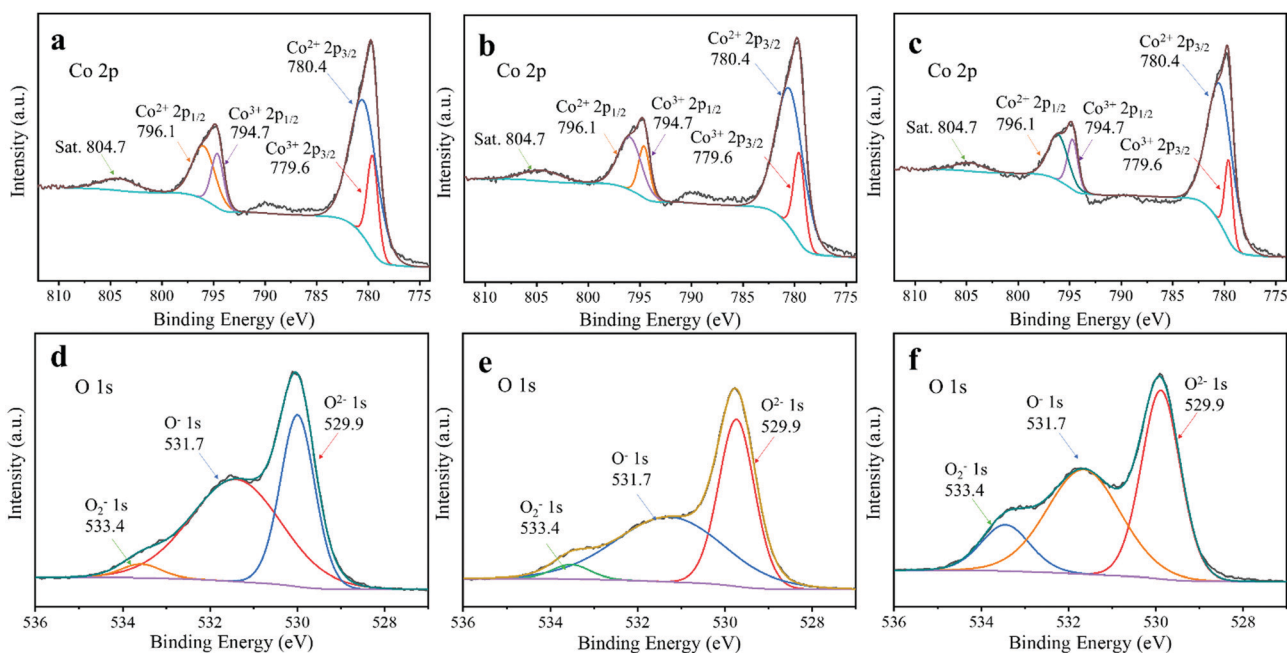

Fig. 4 High resolution (a–c) Co 2p and (d–f) O 1s XPS spectra of (a and d) Co_3O_4-7:2, (b and e) Co_3O_4-4:1 and (c and f) Co_3O_4-9:1.

262 | *Mater. Chem. Front.*, 2021, **5**, 259–267

This journal is © The Royal Society of Chemistry and the Chinese Chemical Society 2021

respectively, which was consistent with the previous study that Co^{2+} was the dominant species in the (111) plane.[65] Besides, a high content of Co^{2+} facilitates the formation of active sites for the OER.[60]

The high resolution XPS spectra of O 1s of Co_3O_4-7 : 2, Co_3O_4-4 : 1 and Co_3O_4-9 : 1 were also obtained, which clearly displayed three oxygen contributions, as illustrated in Fig. 4d–f. The peak at around 529.9 eV is assigned to the metal oxygen bond, while the other two peaks centred at 531.7 and 533.4 eV belong to the chemosorbed oxygen species.[61] The chemosorbed species centred at 533.4 eV is ascribed to the high binding energy peak from surface oxygen defect species, implying the existence of oxygen vacancies on the surface of the samples.[66] Based on the peak areas of different oxygen species in Fig. 4f, we calculated that the relative content of oxygen vacancies of Co_3O_4-9 : 1 was 13%, which was much higher than that of Co_3O_4-4 : 1 (4.0%) and Co_3O_4-7 : 2 (4.2%). The high content oxygen vacancy of Co_3O_4-9 : 1 might be due to the high content of Co^{2+} resulting from the lack of oxygen during calcination.[60] Because the oxygen vacancy is the active site for the OER,[24,35] electrochemical measurements were conducted to evaluate the catalytic activities of Co_3O_4-7 : 2, Co_3O_4-4 : 1 and Co_3O_4-9 : 1.

The electrochemical measurements for the OER were carried out using a standard three-electrode system in oxygen-saturated 1.0 M KOH aqueous solution with the Ag/AgCl electrode as a reference electrode and the Pt wire electrode as a counter electrode. The sample deposited Pt rotating-disk electrode (RDE) with an area of 0.196 cm² was used as a working electrode. Linear sweep voltammetry (LSV) was performed at a scan speed of 0.1 mV s⁻¹ and a rotating speed of 1600 rpm to remove the generated oxygen. First of all, the optimal mass loading was determined by depositing different amounts of Co_3O_4-9 : 1 on the surface of the RDE, as shown in Fig. S6 (ESI†). The LSV curves and Tafel plots indicated the optimal mass loading of 0.38 mg cm⁻² (25 µL), showing a small overpotential of 307 mV and a Tafel slope of 55 mV dec⁻¹ (Fig. S6, ESI†). So the following test for Co_3O_4-7 : 2, Co_3O_4-4 : 1 and Co_3O_4-9 : 1 was carried out at a mass loading of 0.38 mg cm⁻².

Fig. 5a shows the polarization curves of Co_3O_4-7 : 2, Co_3O_4-4 : 1 and Co_3O_4-9 : 1. The peaks at around 1.45 V *vs.* RHE can be ascribed to the oxidation of Co^{2+} to Co^{3+} or Co^{4+}.[67] The Co_3O_4-9 : 1 shows a much lower onset potential (1.49 V *vs.* RHE) than that of Co_3O_4-4 : 1 (1.51 V *vs.* RHE) and Co_3O_4-7 : 2 (1.57 V *vs.* RHE). The overpotential of Co_3O_4-9 : 1 is 307 mV to reach a current density of 10 mA cm⁻², which is lower than that of Co_3O_4-4 : 1 (333 mV) and Co_3O_4-7 : 2 (371 mV), as well as most of the previous reports, as shown in Table S1 (ESI†). The OER kinetics of electrocatalysis was further analysed by Tafel plots. As shown in Fig. 5b, the Tafel slopes of Co_3O_4-9 : 1, Co_3O_4-4 : 1 and Co_3O_4-7 : 2 are 55, 55 and 60 mV dec⁻¹, demonstrating the fast OER catalytic reaction kinetics. The high content of oxygen vacancies of Co_3O_4-9 : 1 was believed to contribute to the enhanced catalytic activity.

The resistances of the samples were obtained by electrochemical impedance spectroscopic (EIS) measurement at a potential of 1.548 V *vs.* RHE, as shown in Fig. 5c. R_{ct} is the charge transfer resistance, which can be estimated from the diameter of the semicircles in the Nyquist plots. The R_{ct} value of Co_3O_4-9 : 1 is the smallest (271 Ω), much lower than that of Co_3O_4-4 : 1 (386 Ω) and Co_3O_4-7 : 2 (584 Ω), respectively, indicating that the OER is easier at the interface of the electrolyte/ electrode of Co_3O_4-9 : 1. We believed that the best conductivity
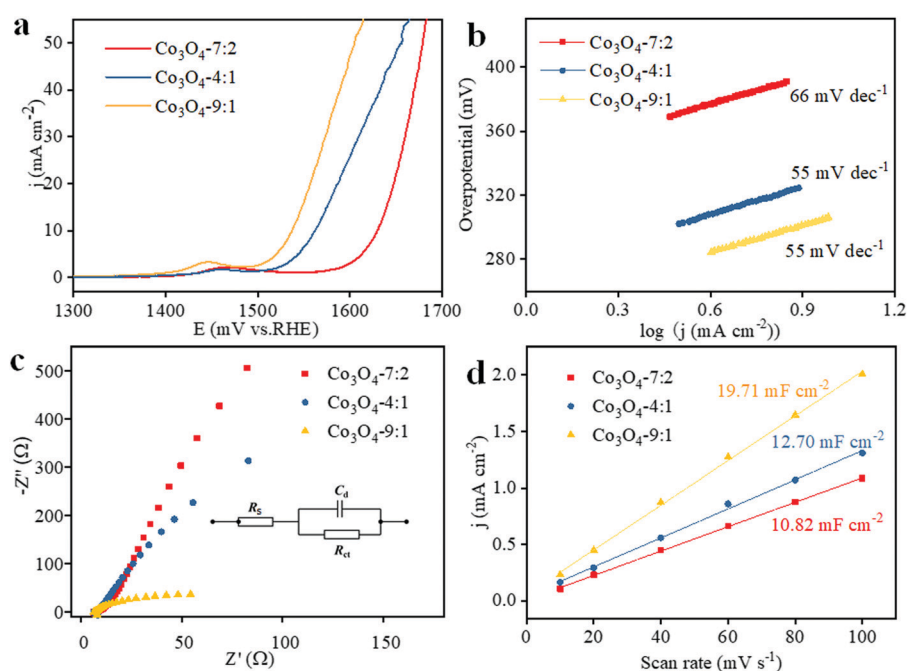

Fig. 5 Electrochemical performance toward the OER. (a) LSV curves, (b) Tafel plots, (c) EIS spectra and (d) capacitive currents as a function of the scan rate to give the double-layer capacitance (C_{dl}) of Co_3O_4-9 : 1, Co_3O_4-4 : 1 and Co_3O_4-7 : 2.

of Co_3O_4-9:1 was contributed by the high content of oxygen vacancies, which supplies more charge carriers compared to the counterparts.[35]

ECSA is a key parameter to determine the catalytic activity of an electrocatalyst, which can be roughly evaluated by the double-layer charging current (C_{dl}).[68,69] As illustrated in Fig. 5d, the linear plots were obtained by the fitting of the current densities and scan rates, presenting a straight line. The current densities were measured at 1.3 V *vs.* RHE from the cyclic voltammetry (CV) curves at different scan rates (10–100 mV s^{-1}) in the region of 1.148–1.348 V *vs.* RHE (no faradaic current is observed). The C_{dl} value of the samples could be estimated from the slope of the fitted lines,[15,70–72] which are calculated to be 19.71, 12.70, and 10.82 mF cm^{-2} for Co_3O_4-9:1, Co_3O_4-4:1 and Co_3O_4-7:2. According to the calculation equation (ECSA = C_{dl}/C_s, C_s is equal to 40 μF cm^{-2} under alkaline conditions),[68,69] the ECSAs of Co_3O_4-9:1, Co_3O_4-4:1 and Co_3O_4-7:2 are calculated to be 129.7, 83.7 and 71.3 m^2 g^{-1}, respectively, considering that the mass loading of the samples is 0.38 mg cm^{-2}. Compared to Co_3O_4-4:1 and Co_3O_4-7:2, the ECSA of Co_3O_4-9:1 was significantly improved, indicating the more exposure of the catalytically active site contributed by oxygen vacancies, which was consistent with the results of XPS. The TOFs of Co_3O_4-9:1, Co_3O_4-4:1 and Co_3O_4-7:2 were calculated to be 4.17, 1.56 and 0.56 s^{-1}, respectively, further confirming the excellent OER performance of Co_3O_4-9:1.

In order to further confirm the contribution of the hollow structure and exposure of the (111) facet of hollow Co_3O_4 dodecahedrons to the OER catalytic activity, the electrochemical properties of Co_3O_4-9:1 were tested after grinding, which destroyed the hollow structure and the dominant exposure of the (111) facet (Fig. 3d).[59] As shown in Fig. S7 (ESI†), the overpotential of Co_3O_4-9:1 increased to 344 mV at 10 mA cm^{-2} after grinding. Besides, the Tafel slope also increased to 68 mV dec^{-1}. The EIS and double layer capacitance were also tested, showing an increased charge transfer resistance (851 Ω) and a decreased ECSA of 29.3 m^2 g^{-1}, much lower than that before grinding (129.7 m^2 g^{-1}). The results demonstrated that the hollow structure and exposure of the (111) facet of Co_3O_4-9:1 supplied more active sites for the OER.

The ECSA-normalized LSV curves are presented in Fig. S8 (ESI†), showing similar results as presented in Fig. 5a. The potential of Co_3O_4-9:1 is 1.544 V at 0.1 mA cm$_{ECSA}$$^{-2}$, which is 14 and 47 mV lower than that of Co_3O_4-4:1 and Co_3O_4-7:2, respectively. The results implied that the high content of oxygen vacancies might optimize the electron structure of Co_3O_4-9:1, which accelerated the charge transfer and the OER process.[73] Overall, the highest catalytic activity of Co_3O_4-9:1 to the OER was determined by several factors including the exposure of the (111) facet, the content of oxygen vacancies, charge transfer resistance and the ECSA. Moreover, Co_3O_4-9:1 also showed reasonable durability, as illustrated in Fig. S9 (ESI†). The overpotential increased 56 mV at a current density of 10 mA cm^{-2} after 1000 cycles compared to the initial overpotential. However, the stability is still far from meeting the requirements of real-world applications. We speculate that the "soft" attached structure of the hollow Co_3O_4 dodecahedrons is not stable enough to guarantee the long term catalytic stability.[59]

4. Conclusions

In summary, we have successfully prepared a series of hollow Co_3O_4 dodecahedrons with controlled exposure of the (111) facet and oxygen vacancies by using ZIF-67 as a precursor and adjusting the atmosphere during calcination, and realized the combination of multiple strategies into one catalytic system for further enhancing the OER performance. Hollow Co_3O_4 dodecahedrons with both controlled exposure of the (111) facets and high content of oxygen vacancies were obtained at a relatively low oxygen partial pressure, which showed an excellent OER performance with an overpotential of 307 mV at 10 mA cm^{-2} and a Tafel slope as low as 55 mV dec^{-1} which is significantly superior to its counterpart with low content of oxygen vacancies obtained at a relatively high oxygen partial pressure or a broken Co_3O_4 dodecahedron being grinded and losing the preferred facets of (111). The excellent OER performance should be attributed to the hollow structure and the effective control of the (111) facets and oxygen vacancies, which allow for more highly active sites and enhanced conductivity.

Conflicts of interest

There are no conflicts to declare.

Acknowledgements

References

1 S. J. Davis, K. Caldeira and H. D. Matthews, Future CO_2 Emissions And Climate Change From Existing Energy Infrastructure, *Science*, 2010, **329**, 1330–1333.

2 Z. Liu, D. Guan, W. Wei, S. J. Davis, P. Ciais, J. Bai, S. Peng, Q. Zhang, K. Hubacek, G. Marland, R. J. Andres, D. Crawford-Brown, J. Lin, H. Zhao, C. Hong, T. A. Boden, K. Feng, G. P. Peters, F. Xi, J. Liu, Y. Li, Y. Zhao, N. Zeng and K. He, Reduced Carbon Emission Estimates From Fossil

264 | *Mater. Chem. Front.*, 2021, **5**, 259–267

This journal is © The Royal Society of Chemistry and the Chinese Chemical Society 2021

Fuel Combustion And Cement Production In China, *Nature*, 2015, **524**, 335–338.

3   S. Bilgen, Structure And Environmental Impact Of Global Energy Consumption, *Renewable Sustainable Energy Rev.*, 2014, **38**, 890–902.

4   Y. Wei, J. Wang, R. Yu, J. Wan and D. Wang, Constructing $SrTiO_3$–TiO_2 Heterogeneous Hollow Multi-Shelled Structures For Enhanced Solar Water Splitting, *Angew. Chem., Int. Ed.*, 2019, **58**, 1422–1426.

5   W.-L. Wang, J. K. Moore, A. C. Martiny and F. W. Primeau, Convergent Estimates Of Marine Nitrogen Fixation, *Nature*, 2019, **566**, 205–211.

6   C. Dong, C. Lian, S. Hu, Z. Deng, J. Gong, M. Li, H. Liu, M. Xing and J. Zhang, Size-Dependent Activity And Selectivity Of Carbon Dioxide Photocatalytic Reduction Over Platinum Nanoparticles, *Nat. Commun.*, 2018, **9**, 1–11.

7   J. Y. Wang, Y. Cui and D. Wang, Design Of Hollow Nanostructures For Energy Storage, Conversion And Production, *Adv. Mater.*, 2019, **31**, 1801993.

8   E. H. M. Salhabi, J. L. Zhao, J. Y. Wang, M. Yang, B. Wang and D. Wang, Hollow Multi-Shelled Structural TiO_{2-x} with Multiple Spatial Confinement For Long-Life Lithium–Sulfur Batteries, *Angew. Chem., Int. Ed.*, 2019, **58**, 9078–9082.

9   J. Y. Wang, J. W. Wan and D. Wang, Hollow Multishelled Structures For Promising Applications: Understanding The Structure-Performance Correlation, *Acc. Chem. Res.*, 2019, **52**, 2169–2178.

10 D. Mao, J. W. Wan, J. Y. Wang and D. Wang, Sequential Templating Approach: A Groundbreaking Strategy To Create Hollow Multishelled Structures, *Adv. Mater.*, 2019, **31**, 1802874.

11 N. T. Suen, S. F. Hung, Q. Quan, N. Zhang, Y. J. Xu and H. M. Chen, Electrocatalysis For The Oxygen Evolution Reaction: Recent Development And Future Perspectives, *Chem. Soc. Rev.*, 2017, **46**, 337–365.

12 T. Rodenas, S. Beeg, I. Spanos, S. Neugebauer, F. Girgsdies, G. Algara-Siller, P. P. M. Schleker, P. Jakes, N. Pfaender, M. Willinger, M. Greiner, G. Prieto, R. Schloegl and S. Heumann, 2D Metal Organic Framework-Graphitic Carbon Nanocomposites As Precursors For High-Performance O_2-Evolution Electrocatalysts, *Adv. Energy Mater.*, 2018, **8**, 1802404.

13 C. Guan, A. Sumboja, H. Wu, W. Ren, X. Liu, H. Zhang, Z. Liu, C. Cheng, S. J. Pennycook and J. Wang, Hollow Co_3O_4 Nanosphere Embedded In Carbon Arrays For Stable And Flexible Solid-State Zinc-Air Batteries, *Adv. Mater.*, 2017, **29**, 1704117.

14 Z. Xue, Y. Li, Y. Zhang, W. Geng, B. Jia, J. Tang, S. Bao, H.-P. Wang, Y. Fan, Z.-W. Wei, Z. Zhang, Z. Ke, G. Li and C.-Y. Su, Modulating Electronic Structure Of Metal–Organic Framework For Efficient Electrocatalytic Oxygen Evolution, *Adv. Energy Mater.*, 2018, **8**, 1801564.

15 L. Liu, H. Wu, J. Li and L. She, Tuning Microstructures Of Iron–Nickel Alloy Catalysts For Efficient Oxygen Evolution Reaction, *Chem. J. Chin. Univ.*, 2020, **41**, 1083–1090.

16 H. Xu, J. Cao, C. Shan, B. Wang, P. Xi, W. Liu and Y. Tang, MOF-Derived Hollow CoS Decorated With CeOx Nanoparticles For Boosting Oxygen Evolution Reaction Electrocatalysis, *Angew. Chem., Int. Ed.*, 2018, **57**, 8654–8658.

17 E. Antolini, Iridium As Catalyst And Cocatalyst For Oxygen Evolution/Reduction In Acidic Polymer Electrolyte Membrane Electrolyzers and Fuel Cells, *ACS Catal.*, 2014, **4**, 1426–1440.

18 Y. Lee, J. Suntivich, K. J. May, E. E. Perry and Y. Shao-Horn, Synthesis And Activities Of Rutile IrO_2 And RuO_2 Nanoparticles For Oxygen Evolution In Acid And Alkaline Solutions, *J. Phys. Chem. Lett.*, 2012, **3**, 399–404.

19 J. Shan, C. Guo, Y. Zhu, S. Chen, L. Song, M. Jaroniec, Y. Zheng and S.-Z. Qiao, Charge-Redistribution-Enhanced Nanocrystalline Ru@IrOx Electrocatalysts For Oxygen Evolution In Acidic Media, *Chemistry*, 2019, **5**, 445–459.

20 L. C. Seitz, C. F. Dickens, K. Nishio, Y. Hikita, J. Montoya, A. Doyle, C. Kirk, A. Vojvodic, H. Y. Hwang, J. K. Norskov and T. F. Jaramillo, A Highly Active And Stable $IrOx/SrIrO_3$ Catalyst For The Oxygen Evolution Reaction, *Science*, 2016, **353**, 1011–1014.

21 Y. Sun, L. Yuan, Z. Liu, Q. Wang, K. Huang and S. Feng, Optimization Of Oxygen Evolution Dynamics On RuO_2 *Via* Controlling Of Spontaneous Dissociation Equilibrium, *Mater. Chem. Front.*, 2019, **3**, 1779–1785.

22 J. Mei, T. Liao, G. A. Ayoko, J. Bell and Z. Sun, Cobalt Oxide-Based Nanoarchitectures For Electrochemical Energy Applications, *Prog. Mater. Sci.*, 2019, **103**, 596–677.

23 L. Chen, X. Zuo, S. Yang, T. Cai and D. Ding, Rational Design And Synthesis Of Hollow Co_3O_4@Fe_2O_3 Core-Shell Nanostructure For The Catalytic Degradation Of Norfloxacin By Coupling With Peroxymonosulfate, *Chem. Eng. J.*, 2019, **359**, 373–384.

24 Z. Chen, B. Zhao, Y.-C. He, H.-R. Wen, X.-Z. Fu, R. Sun and C.-P. Wong, $NiCo_2O_4$ Nanoframes With A Nanosheet Surface As Efficient Electrocatalysts For The Oxygen Evolution Reaction, *Mater. Chem. Front.*, 2018, **2**, 1155–1164.

25 C. K. Ranaweera, C. Zhang, S. Bhoyate, P. K. Kahol, M. Ghimire, S. R. Mishra, F. Perez, B. K. Gupta and R. K. Gupta, Flower-Shaped Cobalt Oxide Nano-Structures As An Efficient, Flexible And Stable Electrocatalyst For The Oxygen Evolution Reaction, *Mater. Chem. Front.*, 2017, **1**, 1580–1584.

26 B. Y. Guan, Y. Lu, Y. Wang, M. Wu and X. W. Lou, Porous Iron–Cobalt Alloy/Nitrogen-Doped Carbon Cages Synthesized *Via* Pyrolysis Of Complex Metal–Organic Framework Hybrids For Oxygen Reduction, *Adv. Funct. Mater.*, 2018, **28**, 1706738.

27 J. H. Kim, S.-K. Park, Y. J. Oh and Y. C. Kang, Hierarchical Hollow Microspheres Grafted with Co Nanoparticle-Embedded Bamboo-Like N-Doped Carbon Nanotube Bundles As Ultrahigh Rate And Long-Life Cathodes For Rechargeable Lithium–Oxygen Batteries, *Chem. Eng. J.*, 2018, **334**, 2500–2510.

28 J. Yang, L. Wei, T. Zhao, T. Yang, J. Wang, W. Wu, X. Yang, Z. Li and M. Wu, Hollow Petal-Like Co_3O_4 Nanoflakes As Bifunctional Electrocatalysts through Template-Free Protocol And Structural Controlled Kinetics In Gas Evolution, *Electrochim. Acta*, 2019, **318**, 949–956.

29 X. Wang, L. Yu, B. Y. Guan, S. Song and X. W. Lou, Metal–Organic Framework Hybrid-Assisted Formation of Co₃O₄/Co–Fe Oxide Double-Shelled Nanoboxes For Enhanced Oxygen Evolution, *Adv. Mater.*, 2018, **30**, 1801211.

30 L. Li, T. Tian, J. Jiang and L. Ai, Hierarchically Porous Co₃O₄ Architectures with Honeycomb-Like Structures For Efficient Oxygen Generation from Electrochemical Water Splitting, *J. Power Sources*, 2015, **294**, 103–111.

31 X. Zhou, Z. Liu, Y. Wang and Y. Ding, Facet Effect of Co₃O₄ Nanocrystals on Visible-Light Driven Water Oxidation, *Appl. Catal., B*, 2018, **237**, 74–84.

32 Y. Xu, F. Zhang, T. Sheng, T. Ye, D. Yi, Y. Yang, S. Liu, X. Wang and J. Yao, Clarifying the Controversial Catalytic Active Sites of Co₃O₄ For the Oxygen Evolution Reaction, *J. Mater. Chem. A*, 2019, **7**, 23191–23198.

33 Z. Chen, C. X. Kronawitter and B. E. Koel, Facet-Dependent Activity And Stability of Co₃O₄ Nanocrystals towards the Oxygen Evolution Reaction, *Phys. Chem. Chem. Phys.*, 2015, **17**, 29387–29393.

34 L. Liu, Z. Jiang, L. Fang, H. Xu, H. Zhang, X. Gu and Y. Wang, Probing the Crystal Plane Effect of Co₃O₄ For Enhanced Electrocatalytic Performance toward Efficient Overall Water Splitting, *ACS Appl. Mater. Interfaces*, 2017, **9**, 27736–27744.

35 L. Xu, Q. Jiang, Z. Xiao, X. Li, J. Huo, S. Wang and L. Dai, Plasma-Engraved Co₃O₄ Nanosheets with Oxygen Vacancies And High Surface Area For the Oxygen Evolution Reaction, *Angew. Chem., Int. Ed.*, 2016, **55**, 5277–5281.

36 Z. Y. Wang, D. Y. Luan, F. Y. C. Boey and X. W. Lou, Fast Formation of SnO₂ Nanoboxes with Enhanced Lithium Storage Capability, *J. Am. Chem. Soc.*, 2011, **133**, 4738–4741.

37 X. Y. Lai, J. Li, B. A. Korgel, Z. H. Dong, Z. M. Li, F. B. Su, J. Du and D. Wang, General Synthesis And Gas-Sensing Properties of Multiple-Shell Metal Oxide Hollow Microspheres, *Angew. Chem., Int. Ed.*, 2011, **50**, 2738–2741.

38 Z. H. Dong, X. Y. Lai, J. E. Halpert, N. L. Yang, L. X. Yi, J. Zhai, D. Wang, Z. Y. Tang and L. Jiang, Accurate Control of Multishelled ZnO Hollow Microspheres For Dye-Sensitized Solar Cells with High Efficiency, *Adv. Mater.*, 2012, **24**, 1046–1049.

39 J. Y. Wang, N. L. Yang, H. J. Tang, Z. H. Dong, Q. Jin, M. Yang, D. Kisailus, H. J. Zhao, Z. Y. Tang and D. Wang, Accurate Control of Multishelled Co₃O₄ Hollow Microspheres As High-Performance Anode Materials In Lithium-Ion Batteries, *Angew. Chem., Int. Ed.*, 2013, **52**, 6417–6420.

40 J. Wang, H. Tang, L. Zhang, H. Ren, R. Yu, Q. Jin, J. Qi, D. Mao, M. Yang, Y. Wang, P. Liu, Y. Zhang, Y. Wen, L. Gu, G. Ma, Z. Su, Z. Tang, H. Zhao and D. Wang, Multi-Shelled Metal Oxides Prepared Via an Anion-Adsorption Mechanism For Lithium-Ion Batteries, *Nat. Energy*, 2016, **1**, 16050.

41 M. Tian, L. Wang, J. Wan, X. Lai, X. Wang and D. Wang, Hollow Multi-Shelled Co₃O₄ Dodecahedra For Non-enzymatic Glucose Biosensor, *Chin. Sci. Bull.*, 2019, **64**, 3640–3646.

42 G. Lin, H. Wang, X. Lai, R. Yang, Y. Zou, J. Wan, D. Liu, H. Jiang and Y. Hu, Co₃O₄/N-Doped RGO Nanocomposites Derived from MOFs And Their Highly Enhanced Gas Sensing Performance, *Sens. Actuators, B*, 2020, **303**, 127219.

43 J. Wang, J. Wan, N. Yang, Q. Li and D. Wang, Hollow Multishell Structures Exercise Temporal–Spatial Ordering And Dynamic Smart Behaviour, *Nat. Rev. Chem.*, 2020, **4**, 159–168.

44 H. Sun, Y. Zhu, B. Yang, Y. Wang, Y. Wu and J. Du, Template-Free Fabrication of Nitrogen-Doped Hollow Carbon Spheres For High-Performance Supercapacitors Based on a Scalable Homopolymer Vesicle, *J. Mater. Chem. A*, 2016, **4**, 12088–12097.

45 J. Wang, H. Tang, H. Wang, R. Yu and D. Wang, Multi-Shelled Hollow Micro-/Nanostructures: Promising Platforms For Lithium-Ion Batteries, *Mater. Chem. Front.*, 2017, **1**, 414–430.

46 B. Wang, L. Xu, G. Liu, P. Zhang, W. Zhu, J. Xia and H. Li, Biomass Willow Catkin-Derived Co₃O₄/N-Doped Hollow Hierarchical Porous Carbon Microtubes As an Effective Tri-Functional Electrocatalyst, *J. Mater. Chem. A*, 2017, **5**, 20170–20179.

47 L. Zhang, T. Mi, M. A. Ziaee, L. Liang and R. Wang, Hollow POM@MOF Hybrid-Derived Porous Co₃O₄/CoMoO₄ Nanocages For Enhanced Electrocatalytic Water Oxidation, *J. Mater. Chem. A*, 2018, **6**, 1639–1647.

48 L. Yu, X. Y. Yu and X. W. Lou, The Design And Synthesis of Hollow Micro-/Nanostructures: Present And Future Trends, *Adv. Mater.*, 2018, **30**, 1800939.

49 J. Tang, J. Yao, X. Zhang, L. Ma, T. Zhang, Z. Niu, X. Chen, L. Zhao, L. Jiang and Y. Sun, Multi-Shell Hollow FeP Microspheres As Efficient Electrocatalyst For Hydrogen Evolution at All pH Values, *Chem. J. Chin. Univ.*, 2019, **40**, 2340–2347.

50 H. Sun and X. Lai, Progress In Preparation And Gas-Sensing Application of Hollow Multi-Shell Structured Materials, *Chem. J. Chin. Univ.*, 2020, **41**, 855–871.

51 L. Oar-Arteta, T. Wezendonk, X. Sun, F. Kapteijn and J. Gascon, Metal Organic Frameworks As Precursors For the Manufacture of Advanced Catalytic Materials, *Mater. Chem. Front.*, 2017, **1**, 1709–1745.

52 S. Dang, Q.-L. Zhu and Q. Xu, Nanomaterials Derived from Metal–Organic Frameworks, *Nat. Rev. Mater.*, 2018, **3**, 1–14.

53 Y.-Z. Chen, R. Zhang, L. Jiao and H.-L. Jiang, Metal–Organic Framework-Derived Porous Materials For Catalysis, *Coord. Chem. Rev.*, 2018, **362**, 1–23.

54 H.-F. Wang, L. Chen, H. Pang, S. Kaskel and Q. Xu, MOF-Derived Electrocatalysts For Oxygen Reduction, Oxygen Evolution And Hydrogen Evolution Reactions, *Chem. Soc. Rev.*, 2020, 1414–1448.

55 P. He, J. Zhou, A. Zhou, Y. Dou and J. Li, MOFs-Based Materials For Photocatalytic CO₂ Reduction, *Chem. J. Chin. Univ.*, 2019, **40**, 855–866.

56 J. Chang, G. Xu, L. Hui and Q. Fang, Quinone-Based Covalent Organic Frameworks For Efficient Oxygen Evolution Reaction, *Chem. J. Chin. Univ.*, 2020, **41**, 1609–1614.

57 X. Gao, H. Pan, C. Qiao, F. Chen, Y. Zhou and W. Yang, Construction of HRP Immobilized Enzyme Reactor Based on Hierarchically Porous Meta–Organic Framework And Its

266 | *Mater. Chem. Front.*, 2021, **5**, 259–267

This journal is © The Royal Society of Chemistry and the Chinese Chemical Society 2021

Dye Degradation Application, *Chem. J. Chin. Univ.*, 2020, **41**, 1591–1599.

58 Y. Wu, H. Chen, J. Wang, H. Liu, E. Lv, Z. Zhu, J. Gao and J. Yao, Metal-Organic Framework-Templated Hollow Co_3O_4/C with Controllable Oxygen Vacancies For Efficient Oxygen Evolution Reaction, *ChemNanoMat*, 2020, **6**, 107–112.

59 L. Wang, J. Wan, Y. Zhao, N. Yang and D. Wang, Hollow Multi-Shelled Structures of Co_3O_4 Dodecahedron with Unique Crystal Orientation For Enhanced Photocatalytic CO_2 Reduction, *J. Am. Chem. Soc.*, 2019, **141**, 2238–2241.

60 W. T. Koo, S. Yu, S. J. Choi, J. S. Jang, J. Y. Cheong and I. D. Kim, Nanoscale PdO Catalyst Functionalized Co_3O_4 Hollow Nanocages Using MOF Templates For Selective Detection of Acetone Molecules In Exhaled Breath, *ACS Appl. Mater. Interfaces*, 2017, **9**, 8201–8210.

61 C. Zhang, F. Zheng, Z. Zhang, D. Xiang, C. Cheng, Z. Zhuang, P. Li, X. Li and W. Chen, Fabrication of Hollow Pompon-Like Co_3O_4 Nanostructures with Rich Defects And High-Index Facet Exposure For Enhanced Oxygen Evolution Catalysis, *J. Mater. Chem. A*, 2019, **7**, 9059–9067.

62 C. Jiao, Z. Wang, X. Zhao, H. Wang, J. Wang, R. Yu and D. Wang, Triple-Shelled Manganese–Cobalt Oxide Hollow Dodecahedra with Highly Enhanced Performance For Rechargeable Alkaline Batteries, *Angew. Chem., Int. Ed.*, 2019, **58**, 996–1001.

63 C. Wang, J. Wang, W. Hu and D. Wang, Controllable Synthesis of Hollow Multishell Structured Co_3O_4 with Improved Rate Performance And Cyclic Stability For Supercapacitors, *Chem. J. Chin. Univ.*, 2020, **36**, 68–73.

64 Q. Liang, H. Jin, Z. Wang, Y. Xiong, S. Yuan, X. Zeng, D. He and S. Mu, Metal-Organic Frameworks Derived Reverse-Encapsulation Co–Nc@Mo_2C Complex For Efficient Overall Water Splitting, *Nano Energy*, 2019, **57**, 746–752.

65 Q. Liu, Z. Chen, Z. Yan, Y. Wang, E. Wang, S. Wang, S. Wang and G. Sun, Crystal-Plane-Dependent Activity of Spinel Co_3O_4 Towards Water Splitting And the Oxygen Reduction Reaction, *ChemElectroChem*, 2018, **5**, 1080–1086.

66 W. Xu, W. Xie and Y. Wang, Co_3O_{4-x}-Carbon@$Fe_{2-y}Co_yO_3$ Heterostructural Hollow Polyhedrons For the Oxygen Evolution Reaction, *ACS Appl. Mater. Interfaces*, 2017, **9**, 28642–28649.

67 H. Liang, F. Meng, M. Cabán-Acevedo, L. Li, A. Forticaux, L. Xiu, Z. Wang and S. Jin, Hydrothermal Continuous Flow Synthesis And Exfoliation of NiCo Layered Double Hydroxide Nanosheets For Enhanced Oxygen Evolution Catalysis, *Nano Lett.*, 2015, **15**, 1421–1427.

68 P. Chen, K. Xu, Z. Fang, Y. Tong, J. Wu, X. Lu, X. Peng, H. Ding, C. Wu and Y. Xie, Metallic Co_4N Porous Nanowire Arrays Activated by Surface Oxidation As Electrocatalysts For the Oxygen Evolution Reaction, *Angew. Chem., Int. Ed.*, 2015, **54**, 14710–14714.

69 C. G. Morales-Guio, L. Liardet and X. Hu, Oxidatively Electrodeposited Thin-Film Transition Metal (Oxy) Hydroxides As Oxygen Evolution Catalysts, *J. Am. Chem. Soc.*, 2016, **138**, 8946–8957.

70 H. Xu, Z.-X. Shi, Y.-X. Tong and G.-R. Li, Porous Microrod Arrays Constructed by Carbon-Confined NiCo@$NiCoO_2$ Core@Shell Nanoparticles As Efficient Electrocatalysts For Oxygen Evolution, *Adv. Mater.*, 2018, **30**, 1705442.

71 M. Li, K. Duanmu, C. Wan, T. Cheng, L. Zhang, S. Dai, W. Chen, Z. Zhao, P. Li, H. Fei, Y. Zhu, R. Yu, J. Luo, K. Zang, Z. Lin, M. Ding, J. Huang, H. Sun, J. Guo, X. Pan, W. A. Goddard, P. Sautet, Y. Huang and X. Duan, Single-Atom Tailoring of Platinum Nanocatalysts For High-Performance Multifunctional Electrocatalysis, *Nat. Catal.*, 2019, **2**, 495–503.

72 J. Zhao, M. Yang, N. Yang, J. Wang and D. Wang, Hollow Micro-/Nanostructure Reviving Lithium–Sulfur Batteries, *Chem. J. Chin. Univ.*, 2020, **36**, 313–319.

73 H. Wang, J. Qi, N. Yang, W. Cui, J. Wang, Q. Li, Q. Zhang, X. Yu, L. Gu, J. Li, R. Yu, K. Huang, S. Song, S. Feng and D. Wang, Dual-Defects Adjusted Crystal-Field Splitting of $LaCo(1-x)Ni(x)O(3-\delta)$ Hollow Multishelled Structures For Efficient Oxygen Evolution, *Angew. Chem., Int. Ed.*, 2020, **59**, 19691–19695.

This journal is © The Royal Society of Chemistry and the Chinese Chemical Society 2021

Mater. Chem. Front., 2021, **5**, 259–267 | **267**